Materials Horizons

ROYAL SOCIETY OF CHEMISTRY

COMMUNICATION

Published on 13 October 2026
Licence and permissions

Check for updates

Cite this: DOI: 10.1039/d6mh01357k

Received 2nd July 2026,
Accepted 12th October 2026

DOI: 10.1039/d6mh01357k

rsc.li/materials-horizons

Co-optimizing photodeformation and stiffness in azobenzene polyimides for enhanced photoinduced stress and multimodal sensing

Xingpeng Chai, Menghan Zhang, Dandan Xu, Zehao Wang, Jia Wei * and Yanlei Yu *

Photomechanical-to-electrical conversion offers an alternative pathway for optical sensing, but reliable and highly linear signals require large and reproducible photoinduced stress. Achieving such mechanical output remains challenging because efficient photodeformation and a high elastic modulus are often difficult to reconcile through molecular design. Herein, the backbone architecture of azobenzene polyimides (azoPIs) was systematically engineered by varying the dianhydride structure while maintaining identical azobenzene content and flexible-segment fraction. Among the resulting polymers, the 6FDA-based azoPI (azoPI-6FDA) exhibits the most favorable combination of mechanical stiffness and photodeformation (E = 3.27 GPa and a bending angle of 75° under UV irradiation) and possesses a high photoinduced stress of 2.0 MPa. AzoPI-6FDA was subsequently integrated with PVDF-TrFE to construct flexible photomechanical-to-electrical sensing devices in both laminated and coaxial fiber configurations. In the laminated device, photoinduced stress generated by azoPI-6FDA was transferred to PVDF-TrFE and converted into a piezoelectric voltage of up to 9.0 V. Both the photoinduced stress and electrical output exhibited nearly linear dependences on UV intensity, with correlation coefficients approaching 0.99, enabling quantitative optical sensing. The coaxial electrospun membrane combined stable electrical output with an elongation at break exceeding 200% and maintained reliable sensing performance under bending. Moreover, UV irradiation generated predominantly unipolar voltage signals, whereas mechanical loading and unloading produced characteristic bipolar piezoelectric signals, allowing direct discrimination between optical and mechanical stimuli without additional signal processing. This work connects molecular backbone design with photoinduced stress generation and device-level signal transduction, providing a robust materials strategy for flexible, self-powered multimodal sensing.

College of Smart Materials and Future Energy and State Key Laboratory of Molecular Engineering of Polymers, Fudan University, Shanghai 200438, P. R. China. E-mail: weijia@fudan.edu.cn, ylyu@fudan.edu.cn

New concepts

Photomechanical-to-electrical conversion provides an alternative pathway for self-powered optical sensing by coupling light-responsive materials with piezoelectric transducers. However, reliable and highly linear signal transduction requires photoactive materials capable of generating large and reproducible photoinduced stress. Achieving such mechanical output remains challenging because large photoinduced stress requires both efficient photodeformation and a high elastic modulus, two properties that are often difficult to reconcile through molecular design. Previous azoPI photomechanical studies have predominantly followed a deformation-centric design paradigm, exploiting either polarization-dependent *trans–cis–trans* reorientation under blue light or *trans-to-cis* photoisomerization under UV irradiation, with a primary focus on photomechanical actuation where bending amplitude is the central performance metric. This work establishes a device-oriented design principle that shifts the focus from maximizing photodeformation alone to co-optimizing photodeformation and stiffness for the generation of device-relevant photoinduced stress. This concept is realized through backbone engineering of azobenzene-containing polyimides, where rigid aromatic segments provide a mechanical constraint for stress generation, while sterically induced free volume preserves the molecular mobility required for azobenzene photoisomerization. The resulting stress-mediated transduction produces a highly linear optical-to-electrical response. Moreover, differences in stress evolution under optical and mechanical inputs are intrinsically encoded as unipolar and bipolar voltage waveforms, enabling direct stimulus discrimination without additional signal processing. This design principle provides a general materials framework for designing photomechanical systems according to device-relevant mechanical output and information-transduction requirements.

1. Introduction

Biological sensory systems are not passive recipients of stimuli, but adaptive interfaces capable of perceiving and transducing diverse external cues, such as light, heat, and mechanical forces, into feedback information for self-regulation and environmental adaptation.[1–6] Inspired by this principle, artificial soft sensing systems are evolving from single-mode stimulus detection toward integrated multimodal platforms that can

perceive, transduce, and respond to external stimuli in a biomimetic manner.[7–15] In this context, light-responsive soft materials have attracted significant attention because light provides wireless, non-contact, spatiotemporally programmable, and remotely addressable stimulation.[16–21] Notably, photodeformable polymers enable controllable macroscopic deformation upon light irradiation through molecular-scale responses. When coupled with electroactive components, the resulting deformation and mechanical stress can be further converted into electrical signals, providing an alternative pathway for optical sensing and enabling bioinspired photomechanical sensing systems.[22–24] For quantitative optical detection, however, the light-responsive material must generate stable and reproducible mechanical output that can be reliably translated into an electrical response.

Azobenzene-containing polymers represent one of the most versatile platforms for constructing light-responsive soft actuators and sensors, as the reversible *trans–cis* photoisomerization of azobenzene chromophores can induce molecular rearrangement within polymer matrices and ultimately generate macroscopic deformation.[25–29] In particular, azobenzene-containing liquid crystal polymers (azo-LCPs) have been widely explored because the cooperative alignment of mesogens efficiently amplifies molecular isomerization into diverse actuation behaviors, such as bending, oscillation, crawling, and rotation.[30–36] Beyond actuation, recent efforts demonstrated that azobenzene-driven deformation can serve as an intermediate mechanical stimulus for electrical output generation. For example, azo-LCPs/polyurethane composite fiber membranes incorporating ionic liquids have been used to convert photoinduced deformation into ion-migration-induced electrical signals for ultraviolet sensing.[37] Further integration with poly(vinylidene fluoride-trifluoroethylene) (PVDF-TrFE) has enabled enhanced sensing performance through the coupling of resistive and piezoelectric responses.[38] In addition, linear liquid crystal polymers combined with PVDF-TrFE have been employed to realize light-to-mechanical-to-electrical signal transduction, providing opportunities for bioinspired information exchange among artificial sensory systems, neurons, the retina, and external environments.[39,40]

Despite these advances, most reported azobenzene liquid crystal polymers rely on flexible spacers or soft segments to facilitate mesogen reorientation and large photodeformation. Although these molecular designs are effective for producing visible deformation, they generally reduce elastic moduli and promote mechanical relaxation. Consequently, a large deformation does not necessarily result in a large mechanical output. For photomechanical-to-electrical sensing, photoinduced stress represents a key performance metric because it determines the mechanical input available to the electroactive component. Large photoinduced stress requires both efficient photodeformation and a sufficiently high elastic modulus, yet the molecular mobility that favors azobenzene photoisomerization commonly conflicts with the structural rigidity required for stress accumulation. Reconciling these two properties, therefore, represents a central materials challenge for stable and highly linear photomechanical signal transduction.

Polyimides (PIs) represent an attractive class of materials because their rigid aromatic backbones endow them with high elastic modulus, excellent thermal stability, and resistance to mechanical relaxation. Incorporating azobenzene units into PI backbones provides a pathway to combine photodeformability with the load-bearing capability required for photoinduced stress generation. However, the rigid backbone and strong intermolecular interactions of PIs, while beneficial for mechanical and thermal robustness, often limit segmental mobility and thus constrain photomechanical deformation and response kinetics.[41–43] To enhance photodeformation performance, molecular design strategies have been explored to introduce flexible segments or increase chain mobility; however, these approaches typically compromise the intrinsic thermal and mechanical advantages of PIs.[44–47] Therefore, co-optimizing photodeformation and stiffness to achieve high photoinduced stress remains a central challenge in the development of azobenzene polyimide (azoPI) actuators and sensors.

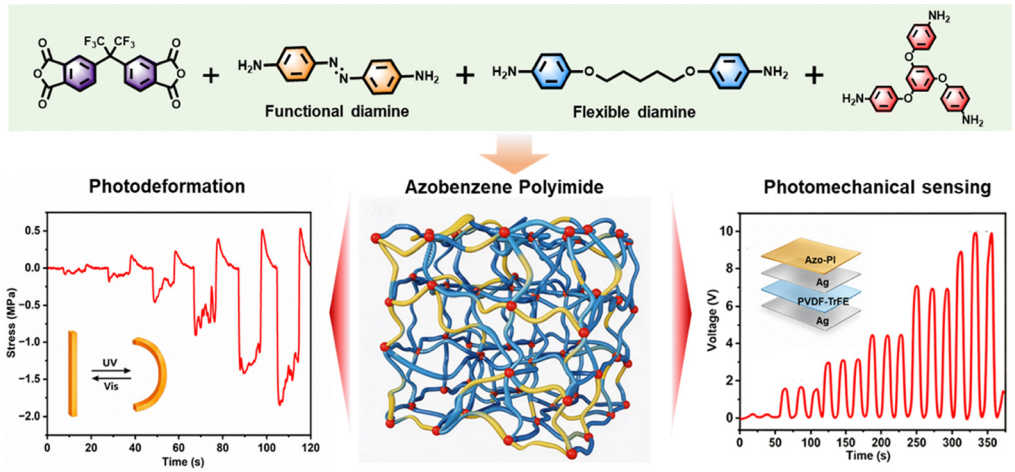
Previous azoPI photomechanical systems have mainly relied on either polarization-selective azobenzene reorientation under linearly polarized blue light or *trans*-to-*cis* photoisomerization under UV irradiation. Despite these different photoactivation pathways, achieving pronounced photodeformation while retaining sufficient mechanical stiffness for efficient generation of photoinduced stress remains challenging. Herein, we address this challenge through a backbone engineering strategy for azobenzene polyimides constructed *via* multicomponent copolymerization, in which the dianhydride structure is systematically varied while maintaining identical azobenzene content and flexible-segment fraction. Among the investigated polymers, the 4,4′-(hexafluoroisopropylidene)diphthalic anhydride-based azoPI (azoPI-6FDA) exhibits the most favorable combination of stiffness and photodeformation, with a high photoinduced stress. Leveraging this optimized material, flexible photomechanoelectric sensing devices were developed by integrating azoPI-6FDA with PVDF-TrFE in both laminated and electrospun fiber architectures, enabling light- and pressure-responsive electrical outputs. The devices exhibit distinct and reversible responses to ultraviolet irradiation and mechanical pressure, demonstrating their potential for multimodal sensing applications. This work connects molecular backbone architecture with photoinduced stress generation and signal transduction, providing a device-oriented materials design strategy for flexible multimodal sensing (Scheme 1).

2. Results and discussion

2.1. Molecular design, synthesis and characterization of multicomponent copolymer azoPIs

Based on the backbone engineering strategy proposed above, four representative dianhydrides with distinct molecular geometries were selected to construct a series of azoPIs while maintaining identical azobenzene content and flexible-segment

 This journal is © The Royal Society of Chemistry 2026



Scheme 1 Schematic illustration of the 6FDA-based azoPI and its photodeformation and photomechanical sensing.

fraction (Fig. 1). The selected dianhydrides, including 6FDA, 2,2-bis[4-(3,4-dicarboxyphenoxy)phenyl]propane dianhydride (BPADA), 4,4′-oxydiphthalic anhydride (ODPA), and 2,3,3′,4′-tetracarboxydiphenyl oxide dianhydride (α-ODPA), differ in fluorination, ether linkage, steric configuration, and structural symmetry, thereby providing a molecular library with systematically varied backbone architectures for subsequent evaluation.

Four freestanding azoPI films were fabricated by spin coating the corresponding polyamic acid precursors, followed by thermal imidization (Fig. 2a), and are hereafter denoted as azoPI-6FDA, azoPI-BPADA, azoPI-ODPA, and azoPI-α-ODPA. The FT-IR spectra (Fig. 2b) exhibited the characteristic absorption bands of the imide groups, including the asymmetric and symmetric stretching vibrations of the imide carbonyl (C═O) groups at 1780 and 1718 cm^{-1}, respectively, along with the

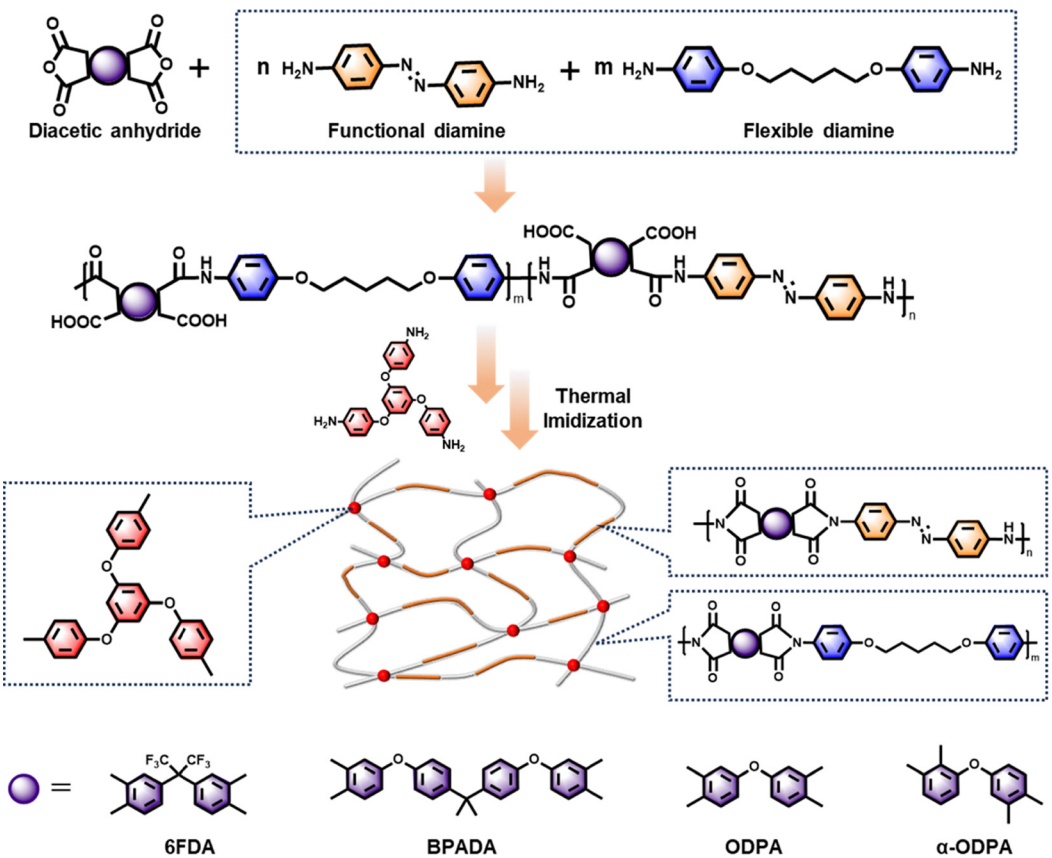


Fig. 1 Synthesis route for the multicomponent copolymer azoPI.

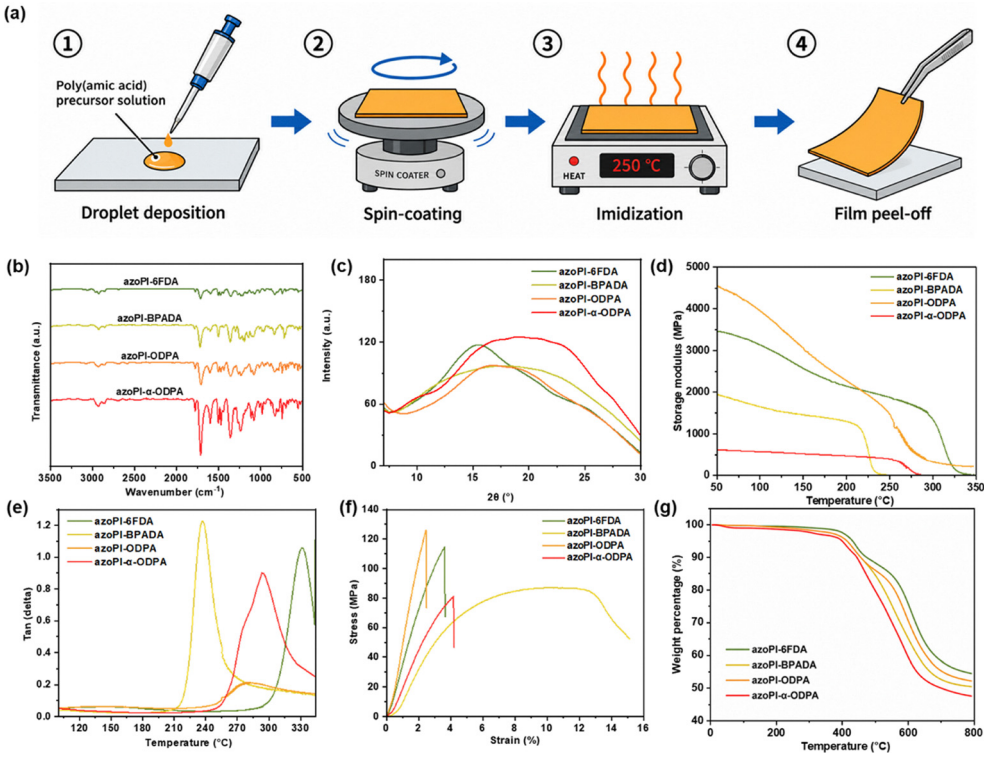


Fig. 2 Structural, mechanical, and thermal characterization of azoPIs with different backbone structures. (a) Schematic illustration of the fabrication process of the azoPI films. (b) FT-IR spectra, (c) one-dimensional WAXD profiles, (d) and (e) DMA, (f) stress–strain and (g) TGA curves of azoPIs.

C–N–C stretching vibration at 1360 cm^{-1}, which confirms the successful formation of the polyimide backbone. No characteristic O–H stretching band associated with residual carboxylic acid groups was observed in the 3300–3500 cm^{-1} region, consistent with the nearly complete imidization of the polyamic acid precursor. Having confirmed the successful formation of the polyimide backbone, the influence of backbone architecture on the molecular packing and physicochemical properties of the resulting azoPIs was subsequently investigated. To assess the possible influence of precursor molecular weight, the soluble polyamic acid (PAA) precursors were characterized by gel permeation chromatography (GPC) before crosslinking (Fig. S1). PAA-6FDA, PAA-BPADA, PAA-ODPA, and PAA-α-ODPA exhibited M_n values of 9.5×10^3, 8.9×10^3, 9.1×10^3, and 7.8×10^3 g mol^{-1}, respectively, with corresponding $Đ$ values of 1.78, 1.82, 1.92, and 1.89, indicating relatively comparable molecular weights and distributions among the four precursors.

Wide-angle X-ray diffraction (WAXD) patterns (Fig. 2c) reveal that all azoPI films are amorphous, as evidenced by broad halos in the 2θ range of 15–25°. Despite the absence of long-range order, systematic variations in short-range packing are clearly observed. The calculated intermolecular chain spacing (d-spacing) follows the order azoPI-ODPA (0.459 nm) < azoPI-α-ODPA (0.509 nm) < azoPI-BPADA (0.533 nm) < azoPI-6FDA (0.573 nm). The progressive increase in d-spacing reflects the distinct steric configurations introduced by different dianhydride structures, indicating that backbone architecture effectively regulates intermolecular packing. Among them, azoPI-6FDA exhibits the largest d-spacing, which is attributed to the bulky hexafluoroisopropylidene groups that reduce packing efficiency. In contrast, azoPI-ODPA possesses the smallest d-spacing, consistent with its relatively compact backbone structure.

While WAXD reveals distinct intermolecular packing among the azoPIs, whether these structural differences lead to consistent variations in thermomechanical behavior remains unclear. Dynamic mechanical analysis (DMA) was therefore performed to probe the segmental dynamics and stiffness of the polymer chains. As shown in Fig. 2d, the glass transition temperature (T_g), determined from the peak of the loss tangent (tan δ) curve, ranges from 247 to 336 °C across the polymer series. AzoPI-6FDA exhibits the highest T_g (336 °C), which can be attributed to the increased energetic barrier for cooperative segmental motion arising from sterically hindered fluorinated substituents. In contrast, the ether-containing polymers exhibit lower T_g values, consistent with reduced constraints on backbone conformational rearrangement due to the rotational flexibility of the ether linkages. The storage modulus (E') curves (Fig. 2e) further reveal distinct differences in stiffness among the polymers. AzoPI-ODPA exhibits the highest storage modulus (4.7 GPa), while azoPI-6FDA also maintains a relatively high value of 3.5 GPa, indicating that both polymers possess superior rigidity in the glassy state. In the present azoPI system, T_g and the storage modulus exhibit different trends, indicating that the underlying thermomechanical behavior results from the combined effects of backbone rigidity, chain packing,

 This journal is © The Royal Society of Chemistry 2026

and segmental flexibility rather than any single structural parameter.

The tensile properties (Fig. 2f, Fig. S2 and Table S1) show a trend that is broadly consistent with the DMA results in terms of relative stiffness. AzoPI-ODPA exhibits the highest tensile strength (128.4 MPa) and Young's modulus (5.9 GPa), corroborating its superior stiffness. In comparison, azoPI-6FDA also maintains a relatively high Young's modulus of 3.27 GPa, whereas the remaining polymers exhibit lower tensile strength and modulus. The thermal stability of the four azoPI films was investigated by thermogravimetric analysis (TGA). As summarized in Fig. 2g and Table S2, all azoPI films show decomposition temperatures above 400 °C, indicating outstanding thermal stability. Notably, azoPI-6FDA exhibits the best thermal resistance, with T_d^5 and T_d^{10} values of approximately 425 and 485 °C, respectively. These results demonstrate that dianhydride selection effectively regulates the backbone stiffness, chain packing, and thermomechanical stability of the azoPIs, providing a mechanical basis for evaluating their subsequent photodeformation and photoinduced stress generation.

2.2. Photodeformation performance of AzoPI films

The above results demonstrate that variation of the dianhydride structure effectively tailors the thermal and mechanical properties of azoPI films by altering their backbone architecture. Because photoinduced stress depends on both the extent of photodeformation and the elastic modulus, neither large deformation nor high stiffness alone is sufficient for maximizing mechanical output. Co-optimizing these competing properties therefore represents a key challenge in the molecular design of azoPIs. Accordingly, the photodeformation behaviors of the resulting films were systematically investigated to identify the backbone architecture that provides the most favorable overall actuation performance.

To quantitatively evaluate the photomechanical performance of the azoPI films, the photoinduced stress generated under UV irradiation was measured. As shown in Fig. 3, strip-shaped specimens (10 mm × 2 mm × 10 μm) were irradiated with 365 nm UV light at an intensity of 120 mW cm^{-2} (Fig. 3a), and the photoinduced stresses of azoPI-6FDA, azoPI-BPADA, azoPI-ODPA, and azoPI-α-ODPA were determined to be 2.0, 1.8, 1.3, and 1.7 MPa, respectively (Fig. 3b). Moreover, the photoinduced stress of azoPI-6FDA remained highly reversible over repeated irradiation cycles without noticeable attenuation in either the response amplitude or profile (Fig. 3c), highlighting its excellent operational stability and photomechanical reliability.

The photodeformation behavior of the azoPI films was further evaluated by monitoring their bending responses under UV exposure. Upon UV irradiation, asymmetric photoisomerization across the film thickness generates a stress gradient that drives macroscopic bending. Among the investigated azoPI films, azoPI-6FDA exhibited the largest bending angle of 75° under UV irradiation (Fig. 3d, e and Fig. S3), indicating the most efficient macroscopic deformation under UV irradiation. UV-vis absorption spectroscopy (Fig. S4) further revealed that azoPI-6FDA possessed favorable photoisomerization kinetics and degree of azobenzene isomerization, providing molecular-level evidence for its enhanced photomechanical response. Overall, azoPI-6FDA delivered the most favorable combination of large photodeformation, reversible stress generation, and robust

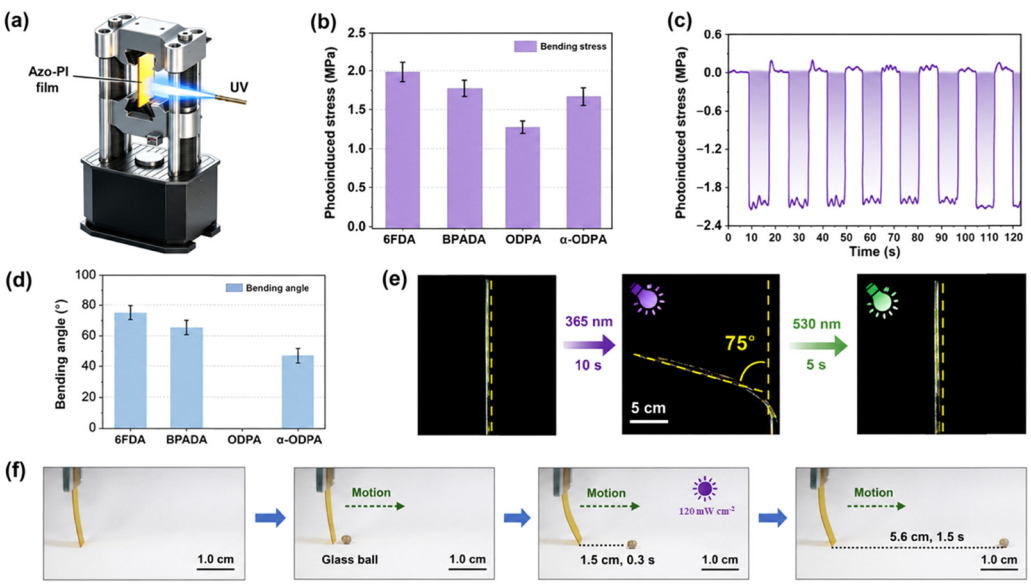


Fig. 3 Photomechanical performance of azoPI films. (a) Schematic illustration of the photoinduced stress measurement setup for azoPI films. (b) Photoinduced stress curves of azoPI films with different backbone structures. (c) Cyclic photoinduced stress response of azoPI-6FDA over consecutive UV on/off cycles. (d) Photoinduced bending angles of azoPI films with different backbone structures. (e) Photodeformation behavior of azoPI-6FDA under 365 nm UV irradiation and recovery behavior under 530 nm green-light irradiation. (f) UV-light-driven transport of a glass bead with a weight 50 times that of the azoPI-6FDA/PE film. All photomechanical tests were conducted with film specimens of 10 mm × 2 mm × 10 μm under an irradiation intensity of 120 mW cm^{-2}.

thermomechanical characteristics. This behavior is attributed to a synergistic balance between a rigid aromatic backbone, which enables effective stress accumulation, and fluorine-induced local free volume, which facilitates azobenzene isomerization within a constrained polymer matrix. Notably, azoPI-ODPA exhibits the highest stiffness but a comparatively low photoinduced stress, whereas azoPI-6FDA combines relatively high stiffness with the largest bending response and consequently generates the highest photoinduced stress. This comparison indicates that photoinduced stress is governed by the combined contributions of stiffness and photodeformation rather than either property alone. To provide a more systematic quantitative comparison, the mechanical and photomechanical parameters of the four azoPI films are summarized in Table S1. A normalized stiffness-photodeformation index, defined as the product of Young's modulus and bending angle, was further correlated with photoinduced stress (Fig. S5). The resulting positive correlation (R^2 = 0.957) further supports that efficient photoinduced-stress generation requires a favorable balance between mechanical stiffness and photodeformation capability.

Owing to its superior overall performance, azoPI-6FDA was selected for actuator demonstration. The azoPI-6FDA film was integrated with a polyethylene (PE) layer to construct a bilayer "kickball" actuator (Fig. 3f). Under UV irradiation, the asymmetric photogenerated stress in the azoPI-6FDA layer drives rapid bending of the bilayer actuator. The passive PE layer converts the in-plane photoinduced stress into amplified bending deformation while simultaneously providing an elastic restoring force, enabling rapid recovery within approximately 5 s after light is switched off. The actuator can repeatedly propel a glass bead with a mass approximately 50 times that of the bilayer actuator under UV irradiation, highlighting its ability to generate large mechanical output under light stimulation.

2.3. Photomechanically driven piezoelectric response of the azoPI-6FDA/PVDF-TrFE bilayer device

To evaluate the potential of azoPI-6FDA for self-powered optical sensing, its favorable combination of photodeformation, stiffness, and thermomechanical stability, together with the resulting large and reversible photoinduced stress, was leveraged to construct a hybrid piezoelectric device. As illustrated in Fig. 4a, the azoPI-6FDA/PVDF-TrFE bilayer device was fabricated *via* sequential spin-coating of PVDF-TrFE, magnetron sputtering of Ag electrodes, and electrostatic bonding of the azoPI-6FDA layer (Fig. S6). The cross-sectional SEM image confirms intimate interfacial contact between the two layers, which is expected to facilitate mechanical stress transfer across the interface. The working mechanism is illustrated in Fig. 4b. Upon 365 nm UV irradiation, azobenzene *trans–cis* isomerization in the azoPI-6FDA layer induces photodeformation, which generates photoinduced stress that is mechanically transferred to the PVDF-TrFE layer, leading to charge redistribution and electrical output *via* the piezoelectric effect.

The photomechanical response of azoPI-6FDA was further quantified as a function of light intensity. As shown in Fig. 4c and Fig. S7, the generated stress increases with increasing UV

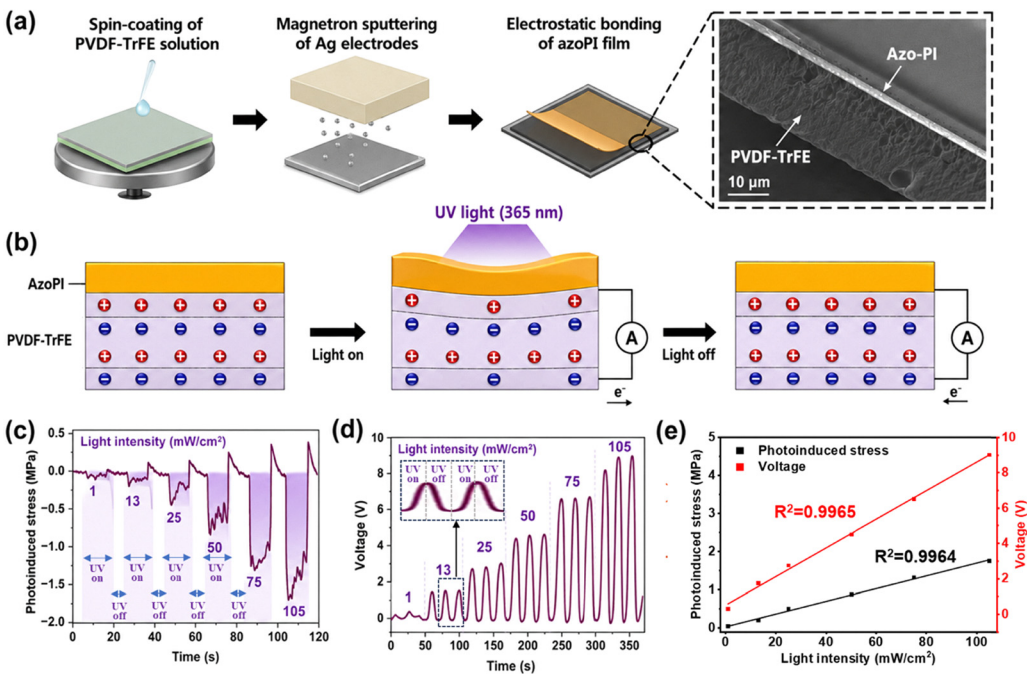


Fig. 4 Fabrication, working mechanism and optoelectrical characterization of the azoPI-6FDA/PVDF-TrFE composite device. (a) Fabrication and SEM image of azoPI-6FDA/PVDF-TrFE. (b) Mechanism of photomechanical-to-electrical conversion in the device. (c) Photoinduced stress of azoPI-6FDA and (d) voltage signal values from azoPI-6FDA/PVDF-TrFE under different light intensities. (e) Light intensity-dependent photoinduced stress and piezoelectric responses, with R^2 values of 0.9964 and 0.9965, respectively. The light intensities are 1, 13, 25, 50, 75, and 105 mW cm^{-2}, and the device size is 5 mm × 5 mm.

This journal is © The Royal Society of Chemistry 2026

intensity, indicating tunable mechanical output under optical stimulation. At 105 mW cm^{-2}, a photoinduced stress of ~1.8 MPa is achieved, while measurable stress is still observed at lower intensities. The electrical response of the bilayer device was then investigated under cyclic UV irradiation with varying intensities (Fig. 4d and Fig. S7). The output voltage increases monotonically with light intensity, consistent with the stress-dependent piezoelectric response. At 105 mW cm^{-2}, the device delivers a maximum output voltage of ~9.0 V and exhibits stable and reversible switching over light on/off cycles. The photoinduced stress and output voltage both exhibit nearly linear dependences on UV intensity, with R^2 values of 0.9964 and 0.9965, respectively. The close agreement between these correlations indicates that the intensity-dependent photoinduced stress generated by azoPI-6FDA is consistently transferred and faithfully converted into piezoelectric output.

To confirm the dominant photomechanical–piezoelectric origin and rule out interfering contributions, we performed a series of control experiments. First, we monitored the temperature evolution under identical irradiation conditions to assess thermal effects. Even at the highest intensity, the surface temperature only exhibited a moderate rise to ~34.1 °C within 10 s (Fig. S8 and S9). We then conducted a thermal control experiment in the absence of UV irradiation, reproducing the measured ~9 °C temperature increase (from ~25 to 34 °C) within 10 s. Under this matched thermal condition, the resulting voltage was only 0.23 ± 0.01 V, accounting for approximately 2.6% of the UV-induced output, indicating that thermal effects make only a minor contribution (Fig. S10). In addition to the thermal control experiment, we further fabricated and tested a series of control devices to isolate the origin of the electrical output (Fig. S11). Pristine PVDF-TrFE and azoPI-6FDA/unpoled PVDF-TrFE devices exhibited negligible responses; the non-photoresponsive PI/PVDF-TrFE device generated only a weak signal; and the azoPI-6FDA-only device produced no measurable output. The dependence on the poling state was further confirmed by reversing the polarization direction of the PVDF-TrFE layer while keeping the electrode connections and wiring polarity unchanged: the dominant output-voltage polarity reversed correspondingly (Fig. S12), providing direct evidence of the piezoelectric origin. Collectively, these control experiments confirm that the output originates predominantly from photoinduced stress transfer from azoPI-6FDA to the electrically poled PVDF-TrFE layer.

The blue-light-responsive azoPI/PVDF laminated device reported by T. J. White *et al.* represents an important demonstration of photopiezoelectric conversion, in which the azoPI layer generates a photoinduced stress of ~0.12 MPa and the laminated device delivers an electrical output of ~0.006 V under 445 nm irradiation.[48] In comparison, the present azoPI-6FDA layer generates a photoinduced stress of ~1.8 MPa within 10 s under 365 nm UV irradiation, and the integrated azoPI-6FDA/PVDF-TrFE device delivers an output voltage of up to 9.0 V. Moreover, the highly linear intensity-dependent transduction demonstrated here was not established in the previous study, and the optical–mechanical multimodal discrimination presented further distinguishes the present system as an advanced self-powered optical sensing device.

2.4. Fiber-architectured photomechanical–piezoelectric hybrid devices with enhanced flexibility and durability

To improve device flexibility and integrate the photoactive and piezoelectric components at the individual-fiber level, a coaxial electrospun membrane was further developed (Fig. 5a). By optimizing the electrospinning parameters, uniform nanofibers were obtained (Fig. S13). Coaxial electrospinning was employed to fabricate azoPI-6FDA/PVDF-TrFE core–shell nanofibers, in which azoPI-6FDA served as the light-responsive core and PVDF-TrFE acted as the piezoelectric shell (Fig. S14). Compared with conventional laminated films, this coaxial architecture integrates photomechanical actuation and piezoelectric transduction within individual fibers, enabling strain transfer from the photoactive azoPI to the piezoelectric PVDF-TrFE while simultaneously improving structural compliance and interfacial integrity.

As shown in Fig. 5b, the as-prepared membrane exhibits an interconnected fibrous network with fiber morphology. The enlarged image further confirms the core–shell configuration of the composite fiber, indicating successful integration of azoPI-6FDA and PVDF-TrFE within a single fiber structure. The voltage output of the fiber membrane was then investigated under UV irradiation with different light intensities. As shown in Fig. 5c, the output voltage increases progressively with increasing irradiation intensity and reaches approximately 1.2 V at 105 mW cm^{-2}. This intensity-dependent response indicates that the optical input was converted into a tunable electrical signal through photomechanical deformation of the azoPI-6FDA component and subsequent piezoelectric conversion by PVDF-TrFE. Moreover, the device retained approximately 98% of its initial voltage output after 100 and 1000 consecutive UV on/off cycles (Fig. 5d and Fig. S15), without appreciable waveform degradation, demonstrating stable and reversible operation under repeated optical stimulation.

The stretchability and mechanical compliance of the fiber membrane were further evaluated by tensile testing. As shown in Fig. 5e, the membrane exhibits an elongation at break exceeding 200%, which is substantially higher than that of the azoPI-6FDA film, indicating markedly improved stretchability and mechanical compliance. Such compliance is particularly advantageous for flexible and wearable sensing applications, where repeated deformation and conformal contact are required. To further assess its performance under mechanically deformed conditions, the voltage output of the fiber membrane was measured during UV irradiation in both flat and bent states (Fig. 5f). Stable and reproducible voltage output was obtained in both configurations, confirming that the fiber membrane maintains reliable photomechanical-to-electrical conversion under deformation. Interestingly, the bent membrane produces a slightly higher voltage output than the flat membrane, which may be associated with more effective mechanical coupling under the pre-deformed configuration. To evaluate device-level flexibility, the photoinduced electrical

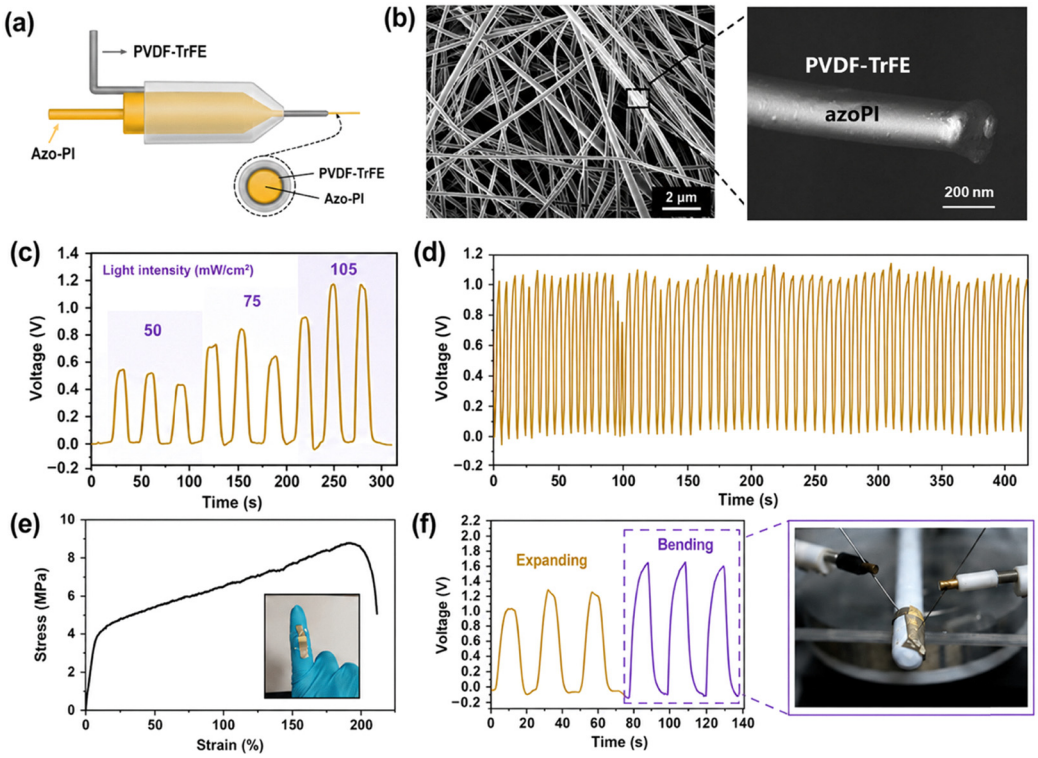


Fig. 5 Preparation and electromechanical properties of coaxial electrospun azoPI-6FDA/PVDF-TrFE fiber membranes. (a) Schematic and (b) SEM images of the coaxial electrospun fiber membrane fabricated from azoPI-6FDA/PVDF-TrFE. (c) Voltage signals of the device under different light intensities and (d) voltage signals under 100 cycles. (e) Stress–strain curve of the freestanding coaxial fiber membrane before ITO electrode deposition. (f) Voltage responses in the flat and bent states.

output of the complete electrode-integrated device was measured at bending radii of 40, 30, 20, and 10 mm (Fig. S16). A clear response was maintained at all tested radii, and the device retained approximately 98.5% of its initial output after ten bending–release cycles at a radius of 10 mm, demonstrating short-term bending repeatability. These results demonstrate that the azoPI-6FDA/PVDF-TrFE fiber membrane combines light responsiveness, mechanical flexibility, and stable electrical output, highlighting its potential for flexible self-powered photomechanical sensing devices.

2.5. Multimodal sensing through distinct electrical responses to optical and mechanical stimuli

Following the demonstration of photomechanical-to-electrical UV sensing, the response of the electrospun membrane to external mechanical stimuli was further investigated to evaluate its capability for multimodal sensing. As shown in Fig. 6, the electrospun membrane generated distinct electrical waveform characteristics under optical and mechanical stimulation. Under UV irradiation, the device produced a unipolar positive voltage signal, and its peak voltage exhibited a clear increase from approximately 0.18–0.20 V to 0.45–0.50 V with increasing light intensity (Fig. 6a–c). In contrast, applied mechanical pressure generated characteristic bipolar piezoelectric signals, consisting of positive and negative voltage peaks during the mechanical loading and unloading processes, respectively (Fig. 6d–f). The device generated detectable bipolar voltage signals over an expanded force range of 0.05–2 N, with clear responses observed even at low forces of 0.05 and 0.1 N (Fig. S17). At applied forces of 1 and 2 N, positive peaks of approximately 0.03–0.04 V and negative peaks ranging from −0.06 to −0.11 V were obtained. These characteristic bipolar waveforms were readily distinguishable from the predominantly unipolar response generated under UV irradiation. The device also maintained a stable output amplitude and waveform over 200 consecutive mechanical loading–unloading cycles (Fig. S18), confirming good repeatability under cyclic mechanical stimulation. To further evaluate multimodal discrimination, optical, mechanical, and simultaneous optical–mechanical stimuli were applied in randomized sequences (Fig. 6g and h). Optical stimulation produced a slowly evolving, predominantly unipolar response, whereas mechanical stimulation generated rapid bipolar transients. The combined input retained both waveform components, allowing the three stimulus modes to be distinguished directly from their temporal and polarity characteristics, irrespective of the input order and without additional signal processing.

The distinct waveform characteristics originate from different signal-generation mechanisms associated with optical and mechanical stimulation. Under UV irradiation, photodeformation of the azoPI layer generates photoinduced stress that is transferred to the PVDF-TrFE layer, leading to a predominantly unipolar voltage output. In contrast, external mechanical loading and unloading induce successive deformation of the

 This journal is © The Royal Society of Chemistry 2026

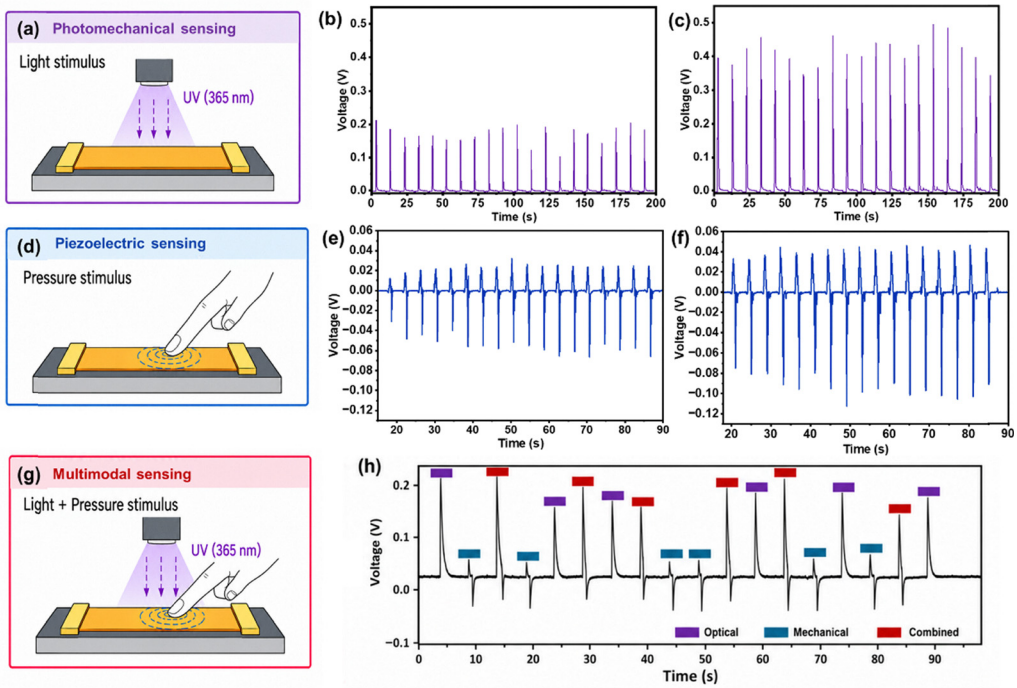


Fig. 6 Multimodal photomechanical and piezoelectric sensing performance of the azoPI-based device. (a) Schematic illustration of the photomechanical sensing mechanism. Cyclic photoinduced piezoelectric voltage response of the device under UV illumination intensities of (b) 25 mW cm^{-2} and (c) 50 mW cm^{-2}, showing intensity-dependent output amplitude and excellent cycling stability. (d) Schematic illustration of the piezoelectric sensing mechanism. Cyclic piezoelectric voltage response of the device under applied pressures of (e) 1 N and (f) 2 N, demonstrating pressure-dependent output and stable cycling performance. (g) Schematic illustration of multimodal sensing under individual or simultaneous optical and mechanical stimulation. (h) Voltage response to a randomized sequence of optical, mechanical, and simultaneous optical–mechanical stimuli, showing distinguishable waveform characteristics for the three input modes. Purple, blue, and red markers indicate optical, mechanical, and combined inputs, respectively.

PVDF-TrFE layer, resulting in opposite polarization changes and characteristic bipolar voltage signals. Consequently, the device enables direct discrimination between optical and mechanical stimuli without additional signal processing. These results demonstrate that the electrospun membrane functions as a flexible multimodal self-powered sensor capable of distinguishing light irradiation and mechanical contact. Such capability is highly attractive for bioinspired perception systems, including wearable artificial skin, soft robotic tactile interfaces, and human–machine interaction, where discrimination among different external stimuli is required.

3. Conclusion

In summary, this work demonstrates a backbone engineering strategy for co-optimizing photodeformation and stiffness in azobenzene polyimides to achieve enhanced photoinduced stress generation. By systematically varying dianhydride structures through multicomponent copolymerization, a family of azoPIs with tunable backbone architecture is established. Among them, azoPI-6FDA exhibits the most favorable combination of stiffness and photodeformation, generating a photoinduced stress of 2.0 MPa. This performance arises from the combined contributions of a rigid aromatic framework and the local free volume introduced by the bulky hexafluoroisopropylidene groups.

Integration of azoPI-6FDA with PVDF-TrFE further translates this material-level photoinduced stress into electrical output through stress-mediated photomechanical-to-electrical conversion. The resulting azoPI-6FDA, when integrated with PVDF-TrFE in both laminated and fiber-architectured devices, enables efficient conversion of photomechanical deformation into piezoelectric output, while also supporting conventional pressure sensing. Importantly, light irradiation and direct mechanical loading produce distinct modes of stress evolution, resulting in predominantly unipolar and characteristic bipolar voltage responses, respectively.

These findings establish the co-optimization of photodeformation and stiffness as a device-oriented materials design principle for generating useful photoinduced stress and provide a promising basis for flexible multimodal sensing.

4. Experimental

4.1. Materials and chemicals

The diamine monomers 1,5-bis(4-aminophenoxy)pentane (DA5MG) and 4,4′-azodianiline (DAAB), and the dianhydride 2,2-bis(3,4-dicarboxyphenyl)hexafluoropropane dianhydride (6FDA), along with the crosslinking agent 1,3,5-tris(4-aminophenoxy)benzene, were obtained from Adamas Company. The remaining dianhydride monomers, including 2,2-bis[4-(3,4-dicarboxyphenoxy)phenyl]propane dianhydride (BPADA),

4,4′-oxydiphthalic anhydride (ODPA), and 2,3,3′,4′-tetracarboxydiphenyl oxide dianhydride (α-ODPA), were purchased from Tianjin Zhongtai Chemical Technology Co., Ltd. Polyvinylidene fluoride trifluoroethylene (PVDF-TrFE) was obtained from Kunshan Hais Electronic Co., Ltd.

4.2. Preparation of azobenzene polymer films

The synthesis route for azobenzene polyimide is shown in Fig. 1. The molar ratio of DAAB to DA5MG is set at 4 : 1. In this system, DAAB serves as the functional unit, with its azobenzene group enabling the photomechanical deformation of the polyimide material, while DA5MG provides the flexible chain segment, enhancing the molecular chain movement induced by the isomerization of the azobenzene group. Next, different dianhydride monomers are added for a ternary copolymerization reaction, maintaining the same molar ratio of the monomers across different materials. For example, when 6FDA is used, 0.0487 g (0.17 mmol) of DA5MG and 0.1486 g (0.7 mmol) of DAAB monomers are added to a 50 mL round-bottom flask. Under an argon atmosphere, 5 mL of DMAc solution is added and stirred until completely dissolved. Then, 0.444 g (1 mmol) of 6FDA monomer is dissolved in an appropriate amount of solvent and added to the reaction solution. The reaction is carried out at room temperature for 12 hours. Afterward, 0.036 g (0.09 mmol) of TAPOB crosslinker is added to the solution, and the reaction continues at room temperature for another 12 hours to obtain the polyamic acid (PAA) solution. The solid content of the solution is maintained at approximately 5% by controlling the monomer-to-solvent ratio.

Next, the PAA solution is drop-cast onto a clean glass substrate and placed on a hot plate. The film is then heated for 1 hour at temperatures of 80 °C, 100 °C, 150 °C, 200 °C, and 250 °C for thermal imidization. Afterward, the film is slowly cooled to room temperature for annealing. Once the annealing is complete, the film is removed by etching with hydrofluoric acid and washed three times with ethanol. Finally, the film is dried in an oven at 80 °C for 2 hours to obtain the polyimide film.

4.3. Fabrication of azoPI-6FDA/PVDF-TrFE composite film-based photodevices

First, a 10% PVDF-TrFE solution is prepared and spin-coated onto a glass substrate. The coated film is annealed at 50 °C for 3 hours to produce the PVDF-TrFE film. Subsequently, silver (Ag) electrodes are deposited on both sides of the PVDF-TrFE film using magnetron sputtering. Finally, after poling under a high electric field of 75 MV m^{-1}, a 5 mm × 5 mm azoPI film is electrostatically laminated onto the surface. The total thickness of the film is approximately 30 μm.

4.4. Fabrication of azoPI-6FDA/PVDF-TrFE coaxial fiber membrane photodevices

First, a certain amount of acetic anhydride (dehydrating agent) and triethylamine (catalyst) with a molar ratio of 2 : 1 is added to the PAA solution of the azoPI for chemical imidization to prepare the azoPI spinning solution. Next, the electrospinning parameters for azoPI are optimized. Under controlled conditions of 40% air humidity, a spinning distance of 10 cm, a voltage of 25 kV, and a spinning rate of 0.5 mL h^{-1}, the solution concentration is varied to observe the resulting structures, as shown in Fig. S13. When the solution concentration is 10%, the electrospun product exhibits bead-on-string structures, indicating that the solution viscosity is too low and lacks sufficient continuity to form stable fibers under the influence of the electric field, leading to fiber breakage during stretching. As the solution concentration increases, the bead structures gradually disappear, and at a concentration of 25%, a fibrous membrane structure is formed.

Subsequently, azoPI-6FDA/PVDF-TrFE is processed through coaxial electrospinning. A layer of conductive fabric is wrapped around the collector. Under an air humidity of 40–50%, a spinning distance of 10 cm, and a voltage of 25 kV, electrospinning is performed at a rate of 1 mL h^{-1} for PVDF-TrFE (shell layer) and 0.5 mL h^{-1} for azoPI (core layer). After 20 minutes, the spun membrane is peeled off along with the conductive fabric. The TEM image in Fig. S14 further confirms that the fibers possess a layered structure, indicating the successful preparation of core–shell fiber membranes. Finally, XRD analysis revealed that the strongest diffraction peak of the fiber membrane is located at 20.2°, corresponding to the β-phase crystalline structure (Fig. S19). The fiber membrane is then cut into 10 mm × 10 mm pieces, and an ITO electrode is deposited on the surface *via* magnetron sputtering to fabricate the device, as illustrated in Fig. S20.

4.5. Characterization

Characterization of specific functional groups in the materials was performed using a Fourier-transform infrared spectrometer (Bruker, VERTEX 70v) with attenuated total reflectance (ATR) technology. The molecular weight and the polydispersity index were measured by gel permeation chromatography (GPC, Waters, E2695) with THF as the eluent at a flow rate of 1 mL min^{-1}. The molecular chain arrangement of the polymer was analyzed using one-dimensional wide-angle X-ray diffractometers (Bruker D8 Advance & Rigaku SmartLab). A thermogravimetric analyzer (TA Q500) was employed to determine the thermal stability of azoPI films, while their thermodynamic properties were evaluated using a dynamic mechanical analyzer (TA Q800). Photodeformation of the films was achieved using a 365 nm ultraviolet light source (OMRON, ZUV-H30MC) and a 530 nm visible light source (CCS, HLV-24GR-3W) as stimuli. A super-depth 3D microscope (Keyence, VHX-7000C) was used to capture deformation under UV light and recovery under visible light. A UV/Vis spectrophotometer (PerkinElmer, Lambda 650) was used to measure the characteristic absorption peaks and photoisomerization capacity of the films. A universal testing machine (Instron, 5567) was used to assess the stress–strain curves and photoinduced stress of the films. For photoinduced stress measurements, azoPI strips (10 mm × 2 mm × 10 μm) were mounted between two rigid flat clamps, with one end fixed and the other connected to the force transducer. After applying a small preload to remove slack, a central area of 3 mm × 2 mm was irradiated with 365 nm UV light, and the

 This journal is © The Royal Society of Chemistry 2026

photoinduced stress was calculated as $\sigma = F/A$, where F is the photoinduced force and A is the specimen cross-sectional area. The force transducer and irradiation intensity were calibrated using standard weights and an optical power meter, respectively. Measurements were conducted at 25 °C and 40% relative humidity, with ten independent measurements performed for each condition.

For the sensor components, the cross-sectional structure of the azoPI-6FDA/PVDF-TrFE composite films and the coaxial electrospun fiber structure were observed using a field-emission scanning electron microscope (Zeiss, Ultra55) and a high-contrast transmission electron microscope (HITACHI, HT7800). Electrospinning of azoPI and azoPI-6FDA/PVDF-TrFE fiber membranes was carried out using an electrospinning system (SS-11). A magnetron sputtering system (Kurt J. Lesker, PVD 75) was used to deposit metal electrodes on both sides of the films. A digital source meter (Keithley, 2602B) was employed to collect the voltage signals of azoPI-6FDA/PVDF-TrFE. For the matched thermal-control experiment, the device was alternately inserted into and removed from an oven, producing an increase in temperature from approximately 25 to 34 °C within 10 s. Note that the oven was preset to ~40 °C, slightly above the target temperature, so that the device could reach 34 °C within the target 10 s heating window. The measurements were repeated over five heating–cooling cycles, and the voltage was recorded in the absence of UV irradiation using the same device configuration and acquisition settings as those used for the UV measurements.

Conflicts of interest

The authors declare no competing financial interests.

Data availability

The data supporting this article have been included as part of the supplementary information (SI). Supplementary information is available. See DOI: https://doi.org/10.1039/d6mh01357k.

Acknowledgements

This work was financially supported by the National Natural Science Foundation of China (No. 22575059, 22595422, and 52073062).

References

1 H. Kong, X. Chen, G. Huang, Y. Long and L. Zhou, Multimodal electronic skin integrating discrete wavelet transform and deep learning for accurate tactile perception, *Adv. Funct. Mater.*, 2026, **36**, 75219.
2 Z. Yu, J. Feng, W. Dou, X. Ge, D. He, M. Zhang, H. Wang and Y. Zhou, Advanced intelligent e-skin: multimodal sensing to ai-driven clinical monitoring, *Mater. Today*, 2026, **93**, 103211.
3 M. Xia, N. Pan, C. Zhang, C. Zhang, W. Fan, Y. Xia, Z. Wang and K. Sui, Self-powered multifunction ionic skins based on gradient polyelectrolyte hydrogels, *ACS Nano*, 2022, **16**, 4714–4725.
4 S. Yang, Y. J. Cao, K. Han, J. T. Guo, P. L. Zheng, L. Y. Wang, T. Cheng, Y. Z. Zhang and W. Y. Lai, Stretchable transparent electrodes based on metal grid hybrids for skin-like multimodal sensing and flexible touch panel, *Nano Energy*, 2025, **139**, 110942.
5 S. Yang, H. Ding, J. Tan, Y. Zhang, Y. Guo, R. Kang, X. Zhu, H. Wang, R. Baughman and Z. Yin, *et al.*, Multifaceted mechanical responsive metamaterials: Mechanisms, fabrications, and applications, *Innovation*, 2026, **7**, 101070.
6 M. Althumayri, R. Das, R. Banavath, L. Beker, A. M. Achim and H. Ceylan Koydemir, Recent Advances in Transparent Electrodes and Their Multimodal Sensing Applications, *Adv. Sci.*, 2024, **11**, 2405099.
7 J. Yang, C. Shen and N. Cheng, From biosensing to perception: Collaborative few-shot learning for explainable digital biomarker identification in high-dimensional biomedical spectra, *Biosens. Bioelectron.*, 2025, **290**, 117980.
8 N. Rohaizad, C. C. Mayorga-Martinez, M. Fojtu, N. M. Latiff and M. Pumera, Two-dimensional materials in biomedical, biosensing and sensing applications, *Chem. Soc. Rev.*, 2021, **50**, 619–657.
9 Q. Li, T. Tan, B. Wang and Z. Yan, Avian-inspired embodied perception in biohybrid flapping-wing robotics, *Nat. Commun.*, 2024, **15**, 9099.
10 G. Gong, Y. Zhou, Q. Li, W. Zhao, S. Geng, H. Li, Y. B. Leng, S. Zhu, G. Ding and Y. Zhai, *et al.*, Bioinspired adaptive sensors: a review on current developments in theory and application, *Adv. Mater.*, 2025, 2505420.
11 Y. Wang, Q. Geng, H. Lyu, W. Sun, X. Fan, K. Ma, K. Wu, J. Wang, Y. Wang and D. Mei, *et al.*, Bioinspired Flexible Hydrogelation with Programmable Properties for Tactile Sensing, *Adv. Mater.*, 2024, **36**, 2401678.
12 T. Sun, W. Yue, T. Sun, H. Niu and Y. Li, A ''one-stone-two-birds'' strategy constructed hybrid wearable device based on chameleon-inspired integrated pressure sensing and visualization, *Adv. Funct. Mater.*, 2025, **35**, 2503841.
13 R. Wu, X. Liu, T. Zhang and Q. Hua, AI-enabled flexible sensing technologies for safety engineering: Materials, devices, and applications, *Nano Energy*, 2026, **157**, 112284.
14 X.-J. Zha, Q.-K. Li, P. Chen, Y. Liu, J. Huang, J.-B. Li and Y. Zhou, Flexible and multimodal sensing platforms for wearable respiratory monitoring: Innovations in materials and systems for precision health, *Chem. Eng. J.*, 2026, **534**, 175026.
15 Y. Liu, Z. Yin, C. Liu, Z. Liu, S. Liu and Q. Zheng, Photocrosslinked polymer dielectrics enabling flexible organic transistor synapses with excellent linearity for neuromorphic applications, *Chem. Eng. J.*, 2025, **507**, 160538.
16 X. Qing, L. Qin, W. Gu and Y. Yu, Deformation of crosslinked liquid crystal polymers by light-from ultraviolet to visible and infrared, *Liq. Cryst.*, 2016, **43**, 2114–2135.
17 T. Ube and T. Ikeda, Photomobile polymer materials with crosslinked liquid-crystalline structures: molecular design,

fabrication, and functions, *Angew. Chem., Int. Ed.*, 2014, **53**, 10290–10299.
18 T. Ikeda, J. i Mamiya and Y. Yu, Photomechanics of liquid-crystalline elastomers and other polymers, *Angew. Chem., Int. Ed.*, 2007, **46**, 506–528.
19 X. Pang, J. a Lv, C. Zhu, L. Qin and Y. Yu, Photodeformable azobenzene-containing liquid crystal polymers and soft actuators, *Adv. Mater.*, 2019, **31**, 1904224.
20 J. Wei and Y. Yu, Photodeformable polymer gels and cross-linked liquid-crystalline polymers, *Soft Matter*, 2012, **8**, 8050–8059.
21 C. J. Barrett, J. i Mamiya, K. G. Yager and T. Ikeda, Photo-mechanical effects in azobenzene-containing soft materials, *Soft Matter*, 2007, **3**, 1249–1261.
22 K. Imato, K. Momota, N. Kaneda, I. Imae and Y. Ooyama, Photoswitchable adhesives of spiropyran polymers, *Chem. Mater.*, 2022, **34**, 8289–8296.
23 C. L. F. Van Beek and B. L. Feringa, Coupled rotary motion in molecular motors, *J. Am. Chem. Soc.*, 2024, **146**, 5634–5642.
24 X. Fu, B. Zhu and X. Hu, Force-triggered atropisomerization of a parallel diarylethene to its antiparallel diastereomers, *J. Am. Chem. Soc.*, 2023, **145**, 15668–15673.
25 Y. Wang, P. Chen, Y. Chen and M. Yeh, Research on advanced photoresponsive azobenzene hydrogels with push-pull electronic effects: a breakthrough in photoswitchable adhesive technologies, *Mater. Horiz.*, 2025, **12**, 227–237.
26 P. De Gennes, Réflexions sur un type de polymères nématiques, *C. R. Hebd. Séances Acad. Sci.*, 1975, **281**, 101.
27 D. J. Broer, R. G. Gossink and R. A. M. Hikmet, Oriented polymer networks obtained by photopolymerization of liquid-crystalline monomers, *Makromol. Chem.*, 1990, **183**, 45–66.
28 H. Finkelmann, E. Nishikawa, G. G. Pereira and M. Warner, A new opto-mechanical effect in solids, *Phys. Rev. Lett.*, 2001, **87**, 015501.
29 J. a Lv, Y. Liu, J. Wei, E. Chen, L. Qin and Y. Yu, Photocontrol of fluid slugs in liquid crystal polymer microactuators, *Nature*, 2016, **537**, 179–184.
30 X. Chai, J. Wei and Y. Yu, Molecular engineering of photodeformable liquid crystal polymers: chemical structure and network topology, *Macromolecules*, 2025, **59**, 7–28.
31 I. Roppolo, A. Chiappone, A. Angelini, S. Stassi, F. Frascella, C. F. Pirri, C. Ricciardi and E. Descrovi, 3D printable light-responsive polymers, *Mater. Horiz.*, 2017, **4**, 396–401.
32 Y. Cao, Y. Wu, Y. Huang, H. Xiang and L. Zhang, Photo/thermal dual-responsive azobenzene-based photosensitive resin for 4D printing, *Chem. Eng. J.*, 2024, **498**, 155140.
33 X. Huang, L. Qin, J. Wang, X. Zhang, B. Peng and Y. Yu, Multiple shape manipulation of liquid crystal polymers containing Diels–Alder network, *Adv. Funct. Mater.*, 2022, **32**, 2208312.
34 T. S. Hebner, M. Podgórski, S. Mavila, T. J. White and C. N. Bowman, Shape permanence in diarylethene-functionalized liquid-crystal elastomers facilitated by thiol-anhydride dynamic chemistry, *Angew. Chem., Int. Ed.*, 2022, **61**, 202116522.
35 C. Zhang, Z. Zhang and X. Liu, Closed-loop recyclable and totally renewable liquid crystal networks with room-temperature programmability and reconfigurable functionalities, *Angew. Chem., Int. Ed.*, 2024, **63**, 202411280.
36 Z. Pei, Y. Yang, Q. Chen, E. M. Terentjev, Y. Wei and Y. Ji, Mouldable liquid-crystalline elastomer actuators with exchangeable covalent bonds, *Nat. Mater.*, 2013, **13**, 36–41.
37 X. Zheng, Y. Jia and A. Chen, Azobenzene-containing liquid crystalline composites for robust ultraviolet detectors based on conversion of illuminance-mechanical stress-electric signals, *Nat. Commun.*, 2021, **12**, 4875.
38 X. Zheng, Z. Liu, R. Wang and A. Chen, Bending-insensitive intrinsically flexible ultraviolet encoding devices based on piezoelectric nanogenerator-supplied liquid crystalline polymer fabrics, *Small*, 2022, **18**, 2202639.
39 B. Peng, X. Chen, G. Yu, F. Xu, R. Yang, Z. Yu, J. Wei, G. Zhu, L. Qin and J. Zhang, *et al.*, A neuron-readable artificial photoreceptor composed of photodeformable liquid crystal polymers and piezoelectric materials, *Adv. Funct. Mater.*, 2023, **33**, 2214172.
40 Y. Jiang, B. Peng, J. Ma, F. Pan, J. Wei, L. Qin, C. Sun and Y. Yu, A flexible arched artificial photoreceptor constructed by photodeformable liquid crystal polymers and its application in vision restoration, *Smart Molecules*, 2026, **4**, 70030.
41 D. H. Wang, J. J. Wie, K. M. Lee, T. J. White and L.-S. Tan, Impact of backbone rigidity on the photomechanical response of glassy, azobenzene-functionalized polyimides, *Macromolecules*, 2014, **47**, 659–667.
42 M. L. Baczkowski, D. H. Wang, D. H. Lee, K. M. Lee, M. L. Smith, T. J. White and L.-S. Tan, Photomechanical deformation of azobenzene-functionalized polyimides synthesized with bulky substituents, *ACS Macro Lett.*, 2017, **6**, 1432–1437.
43 D. H. Wang, K. M. Lee, Z. Yu, H. Koerner, R. A. Vaia, T. J. White and L. S. Tan, Photomechanical response of glassy azobenzene polyimide networks, *Macromolecules*, 2011, **44**, 3840–3846.
44 P. Zhang, Z. Lan, J. Wei and Y. Yu, Photodeformable azobenzene-containing polyimide with flexible linkers and molecular alignment, *ACS Macro Lett.*, 2021, **10**, 469–475.
45 Y. Chen, Q. Liu, P. Theato, J. Wei and Y. Yu, A convenient route to prepare reactive azobenzene-containing liquid crystal polymers and photodeformable fibers, *Adv. Intell. Syst.*, 2021, **3**, 2000254.
46 X. Sun, M. Zhang, J. Wei and Y. Yu, Multiple shape manipulation of azobenzene-containing polyimide by combining shape memory effect, photofixity, and photodeformation, *ACS Macro Lett.*, 2023, **12**, 921–927.
47 X. Sun, J. Wei and Y. Yu, Photoinduced deformation of amorphous polyimide enabled by an improved azobenzene isomerization efficiency, *Polym. Chem.*, 2022, **13**, 5447–5452.
48 J. W. Jeong, D. H. Wang, V. P. Tondiglia, N. V. Tabiryan, R. O. Vergara-Toloza, L. S. Tan and T. J. White, Photopiezoelectric composites of azobenzene functionalized polyimides and polyvinylidene fluoride, *Macromol. Rapid Commun.*, 2014, **35**, 2050–2056.

 This journal is © The Royal Society of Chemistry 2026